



Cite as
Nano-Micro Lett.
(2023) 15:58

One-Step Gas–Solid-Phase Diffusion-Induced Elemental Reaction for Bandgap-Tunable $\text{Cu}_a\text{Ag}_{m1}\text{Bi}_{m2}\text{I}_n/\text{CuI}$ Thin Film Solar Cells

Received: 30 November 2022
Accepted: 31 January 2023
Published online: 2 March 2023
© The Author(s) 2023

Erchuang Fan^{1,2}, Manying Liu¹ ✉, Kangni Yang¹, Siyu Jiang^{1,2}, Bingxin Li¹, Dandan Zhao¹, Yanru Guo¹, Yange Zhang¹, Peng Zhang², Chuantian Zuo³, Liming Ding³ ✉, Zhi Zheng^{1,2} ✉

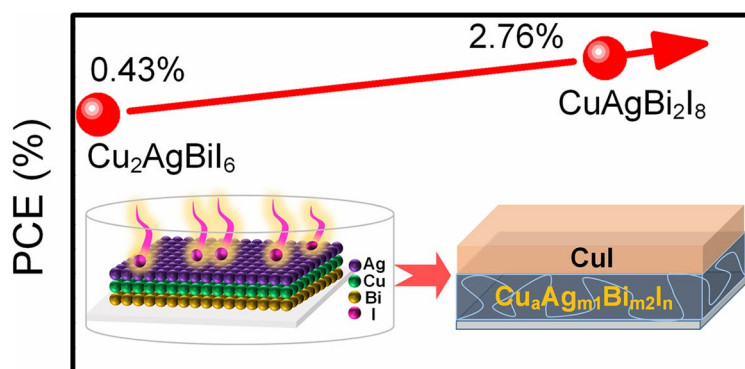
HIGHLIGHTS

- The $\text{Cu}_a\text{Ag}_{m1}\text{Bi}_{m2}\text{I}_n/\text{CuI}$ bilayer films are prepared simultaneously in situ by a one-step low-temperature gas-solid phase diffusion induced elemental reaction without spin coating.
- A new type of $\text{Cu}_a\text{Ag}_{m1}\text{Bi}_{m2}\text{I}_n$ photovoltaic material was originally designed to reduce the bandgap of this class of materials from 2.06 to 1.78 eV by breaking the restriction of double perovskite structure with a ratio of Ag:Bi = 1:1.
- The power conversion efficiency (PCE) of solar cell with a structure of $\text{FTO}/\text{TiO}_2/\text{Cu}_a\text{Ag}_{m1}\text{Bi}_{m2}\text{I}_n/\text{CuI}/\text{carbon}$ reached 2.76%, which is the highest PCE for $\text{Cu}_a\text{Ag}_{m1}\text{Bi}_{m2}\text{I}_n$ absorbers.

ABSTRACT Lead-free inorganic copper-silver-bismuth-halide materials have attracted more and more attention due to their environmental friendliness, high element abundance, and low cost. Here, we developed a strategy of one-step gas–solid-phase diffusion-induced reaction to fabricate a series of bandgap-tunable $\text{Cu}_a\text{Ag}_{m1}\text{Bi}_{m2}\text{I}_n/\text{CuI}$ bilayer films due to the atomic diffusion effect for the first time. By designing and regulating the sputtered Cu/Ag/Bi metal film thickness, the bandgap of $\text{Cu}_a\text{Ag}_{m1}\text{Bi}_{m2}\text{I}_n$ could be reduced from 2.06 to 1.78 eV. Solar cells with the structure of $\text{FTO}/\text{TiO}_2/$

$\text{Cu}_a\text{Ag}_{m1}\text{Bi}_{m2}\text{I}_n/\text{CuI}/\text{carbon}$ were constructed, yielding a champion power conversion efficiency of 2.76%, which is the highest reported for this class of materials owing to the bandgap reduction and the peculiar bilayer structure. The current work provides a practical path for developing the next generation of efficient, stable, and environmentally friendly photovoltaic materials.

KEYWORDS $\text{Cu}_a\text{Ag}_{m1}\text{Bi}_{m2}\text{I}_n$; Elemental reaction; Bandgap tuning; Solar cells; Gas–solid phase



✉ Manying Liu, manyingliu988@xcu.edu.cn; Liming Ding, ding@nanoctr.cn; Zhi Zheng, zzheng@xcu.edu.cn

¹ Key Laboratory of Micro-Nano Materials for Energy Storage and Conversion of Henan Province, College of Chemical and Materials Engineering, Institute of Surface Micro and Nano Materials, Xuchang University, Xuchang 461000, People's Republic of China

² School of Materials Science and Engineering, Zhengzhou University, Zhengzhou 450001, People's Republic of China

³ Center for Excellence in Nanoscience (CAS), Key Laboratory of Nanosystem and Hierarchical Fabrication (CAS), National Center for Nanoscience and Technology, Beijing 100190, People's Republic of China



1 Introduction

Considering comprehensive factors such as element abundance, cost, efficiency, environmental protection, and stability, the research and development of novel photovoltaic materials have never stopped [1–3]. The unique electronic structure of the Pb^{2+} plays a very critical role in the outstanding photovoltaic performances of perovskite materials [4–8], and it could be replaced by a suitable metal or multi-metal combination by a green chemical synthesis strategy, for the construction of environmentally friendly and high-quality inorganic photovoltaic thin films with ideal bandgaps, which have shown great application potential [9–14]. Particularly, isoelectronic Bi^{3+} possesses the same electron arrangement ($6s^26p^0$) and similar ionic radius with Pb^{2+} . From the point of view of the principle of charge balance ($2\text{Pb}^{2+} \rightarrow \text{Ag}^+ + \text{Bi}^{3+}$), the lead-free $\text{Cs}_2\text{AgBiBr}_6$ double perovskite material based on the metal combination of Ag^+ and Bi^{3+} has a good 3D structure, high absorption coefficient ($\approx 10^5 \text{ cm}^{-1}$), long carrier lifetime, and high temperature/humidity stability, which provide the possibility and diversity for designing more ideal light-absorbing materials [10, 12, 15]. However, most of the reported Bi-based inorganic double perovskite materials show indirect bandgaps, and it is difficult to achieve the ideal bandgap values for single-junction solar cells [16].

In recent years, the design and performance optimization of perovskite-like Cu-Ag-Bi-based ternary halide photovoltaic materials with suitable bandgaps, such as CuBiI_4 and $\text{Ag}_{1-3x}\text{Bi}_{1+x}\text{I}_4$, have attracted the attention of researchers [17–19]. However, due to the intrinsic influence of its own structure, the further improvement in both efficiency and stability is limited. In 2021, Rosseinsky's group [20] first reported a novel $\text{Cu}_2\text{AgBiI}_6$ multi-halide photovoltaic material inspired by the design of the double perovskite structure. The material has a direct bandgap of 2.06 eV, an ultra-high optical absorption coefficient of $1.0 \times 10^5 \text{ cm}^{-1}$, a substantial charge-carrier mobility of $1.7 \text{ cm}^2\text{V}^{-1} \text{ s}^{-1}$, and a long photoluminescence lifetime of 33 ns. However, the power conversion efficiency (PCE) is only 0.43% due to the large bandgap and poor film quality. Recently, it was found that the bandgap has little change by varying Cu^+ ion content under the premise of keeping the Ag/Bi atomic ratio (1:1) [21]. Chang et. al. [22] introduced pyridine additives to improve the film quality and got a significant increase

in PCE to 1.00% for $\text{Cu}_2\text{AgBiI}_6$ solar cell devices. And then, the crystallization kinetics of the film was controlled by adding 1.5 vol% HI, which improved the surface coverage and large crystallinity, resulting in an enhanced PCE of 1.3% [23]. As far as we know, the best efficiency of up to 2.39% is achieved by the hot-casting process [24]. Although such a new Cu-Ag-Bi-I-based compound has shown great potential as high-quality photovoltaic material, the current reported bandgap of $\sim 2.0 \text{ eV}$ still greatly deviates from the ideal bandgap [20–22, 25], which is still subject to structural design limitations with Ag/Bi ratio maintaining at 1:1. Another main problem lies in that the non-redox compound reaction among CuI, AgI, and BiI_3 is prone to problems such as the random growth of secondary phases and poor film quality [20, 22–24].

While both free from the influence of lead and beyond the design concept of traditional double perovskite structure (Ag/Bi = 1:1), how to play the role of elemental chemistry to tune the optoelectronic properties of such Cu-Ag-Bi-I based compounds is a huge challenge for researchers. The electron transition from the electron-rich halogen to metal plays an important role in the spectral absorption of ionic crystals. The electron transition from I^- to Bi^{3+} is easier than that from I^- to Ag^+ due to the higher oxidation number (III) of Bi^{3+} . Thus, Bi-I coordination bond can absorb light with a longer wavelength, while the Ag-I coordination bond can absorb a shorter light. As a result, a smaller fraction of silver bismuth and a larger fraction of bismuth octahedra would be beneficial to reduce the bandgap. The fabrication of films based on metal elemental surface reaction is a kind of redox reaction with elemental material sputtered film as raw material, which is beneficial to tune the element ratio and improve the quality of film formation [17, 26–28].

In this work, the intelligently designed lead-free inorganic $\text{Cu}_a\text{Ag}_{m1}\text{Bi}_{m2}\text{I}_n$ absorber layer and the hole transport layer (CuI) were simultaneously fabricated by one-step gas–solid-phase diffusion-induced direct metal surface elemental reaction (DMSER) of copper-silver-bismuth-iodine at a low temperature. The bandgap of $\text{Cu}_a\text{Ag}_{m1}\text{Bi}_{m2}\text{I}_n$ could be reduced to 1.78 eV by modifying the sputtered Cu/Ag/Bi metal film thickness due to the destroy of the Ag/Bi ratio at 1:1. The $\text{CuAgBi}_2\text{I}_8$ solar cell with an FTO/ TiO_2 / $\text{Cu}_a\text{Ag}_{m1}\text{Bi}_{m2}\text{I}_n$ /CuI/carbon structure gained a champion efficiency of 2.76% for the single-junction solar cells. This approach of gas–solid-phase diffusion-induced elemental

reaction is very simple and convenient, which presents a potential pathway to large-scale industrial production of Cu-Ag-Bi-I photovoltaic film materials.

2 Experimental and Characterization

2.1 Materials

The FTO substrates ($1.5 \times 1.5 \text{ cm}^2$, 8Ω) were purchased from Shanghai Zaofu New Materials Co., Ltd. Copper target (99%), bismuth target (99%), silver target (99%) were purchased from Beijing Zhong Cheng Company. Acetone ($\text{C}_3\text{H}_6\text{O}$, 99.5%), isopropanol ($\text{C}_3\text{H}_8\text{O}$, 99.5%), anhydrous ethanol ($\text{C}_2\text{H}_6\text{O}$, 99.5%), and nitric acid (HNO_3 , 68%) were purchased from Sinopharm Chemical Reagent Co., Ltd. Carbon paste was obtained from Shanghai Mater Win New Materials Co., Ltd.

2.2 Fabrication of $\text{Cu}_a\text{Ag}_{m1}\text{Bi}_{m2}\text{I}_n/\text{CuI}$ Thin Film

First, the FTO was ultrasonic cleaned with detergent, deionized water, acetone, isopropanol, and anhydrous ethanol for 30 min, then blow-dried with N_2 , and irradiated with ultraviolet ozone for 30 min to remove organic matter on the surface. Second, 180 nm of Bi, 90 nm of Cu, and 60 nm of Ag thin films were deposited on the treated FTO substrates by a magnetron sputtering instrument under the Ar_2 atmosphere. Third, 0.1 g of I_2 particle and the sputtered Bi/Cu/Ag films were put in a sealed Teflon-lined stainless autoclave and heated at 100°C for 24 h. Finally, a gray-black $\text{CuAgBi}_2\text{I}_8/\text{CuI}$ thin film was obtained on the FTO substrate. $\text{Cu}_{0.7}\text{AgBi}_2\text{I}_{7.7}$ and $\text{Cu}_{0.6}\text{AgBi}_2\text{I}_{7.6}$ thin films were fabricated by using the same procedure except for the thickness of Bi, Cu, and Ag. The Bi, Cu, and Ag thickness of $\text{Cu}_{0.7}\text{AgBi}_2\text{I}_{7.7}$ films is 180, 60, and 60 nm, respectively. The Bi, Cu and Ag thickness of $\text{Cu}_{0.6}\text{AgBi}_2\text{I}_{7.6}$ films is 120, 60, and 60 nm, respectively.

2.3 Preparation of $\text{Cu}_a\text{Ag}_{m1}\text{Bi}_{m2}\text{I}_n$ Thin Film

The pure $\text{Cu}_a\text{Ag}_{m1}\text{Bi}_{m2}\text{I}_n$ film was obtained by etching CuI with $0.5 \text{ mol L}^{-1} \text{ HNO}_3$ for about 14 s.

2.4 Fabrication of $\text{FTO}/\text{c-TiO}_2/\text{m-TiO}_2/\text{Cu}_a\text{Ag}_{m1}\text{Bi}_{m2}\text{I}_n/\text{CuI}/\text{C}$ Solar Cell

The commercial FTO substrates with etched line were ultrasonically cleaned with detergent, deionized water, acetone, isopropanol, and anhydrous ethanol for 30 min in subsequence, then blow-dried with N_2 , and irradiated with ultraviolet ozone for 30 min for removing organic on the substrate surface. 80 μL of c- TiO_2 precursor was spin coated on the treated FTO substrates at the speed of 7000 rpm for 30 s, followed by annealing in air at 500°C for 2 h. The mesoscopic TiO_2 (m- TiO_2) layer was deposited by spin-coating the TiO_2 colloid (30 s, 2000 rpm) and annealing it in air at 450°C for 30 min. After the fabricated TiO_2 layer was treated by UV-ozone for 30 min, three metal monolayer films of Bi, Cu, and Ag metal thin film were sequentially deposited using a magnetron sputtering instrument under Ar atmosphere. And then, the sputtered metal films and iodine pellets were put into a sealed Teflon-lined stainless autoclave and heated at 100°C for 24 h to afford a structure of $\text{FTO}/\text{c-TiO}_2/\text{m-TiO}_2/\text{Cu}_a\text{Ag}_{m1}\text{Bi}_{m2}\text{I}_n/\text{CuI}$ thin film. Finally, the commercial low-temperature conductive carbon paste was scraped onto the above prepared film with a blade and heated at 100°C for 10 min to prepare electrode with the active area of 0.04 cm^2 .

2.5 Characterizations

The X-ray powder diffraction (XRD) patterns were obtained by using an X-ray diffractometer (Bruker, D8-Advanced) with Cu $\text{K}\alpha$ radiation in a step size of 0.02° . Raman spectra were recorded by Raman spectrometer (Renishaw In Via). The X-ray photoelectron spectra (XPS) and ultraviolet photoemission spectra (UPS) were measured via an X-ray photoelectron spectrometer (ESCALAB Xi, Thermo Fisher Scientific). The top-view and cross-sectional morphologies, and element component were investigated through scanning electron microscopy (SEM) with an energy-dispersive X-ray (EDS) (Nova NanoSEM 50). The absorption curves were measured by a UV-vis-NIR spectrophotometer (Cary 5000 UV-Vis, Varian). The time-resolved photoluminescence (TRPL) was collected by a fluorescence spectrophotometer equipped with an excitation wavelength of 465 nm. The TSPV signals were collected by an oscilloscope (Tektronix TDS 3054C, 500 MHz) when the film was irradiated by a

355-nm pulsed laser. Current density–voltage characteristic (J-V) curves were measured in air under AM 1.5G sunlight generated by a solar simulator.

3 Results and Discussion

3.1 Fabrication and Characterization of $\text{Cu}_a\text{Ag}_{m1}\text{Bi}_{m2}\text{I}_n$ Films

A series of $\text{Cu}_a\text{Ag}_{m1}\text{Bi}_{m2}\text{I}_n$ quaternary compound films were prepared by the gas–solid-phase reaction method of copper–silver–bismuth–iodine at low temperature (Fig. 1a). In short, the definite thicknesses of Bi, Cu and Ag metal layers

(the total metal thickness 240–330 nm) were successively sputtered on FTO glass in sequence (Figs. S1–S3), which reacted with excess iodine gas to afford $\text{Cu}_{0.6}\text{AgBi}_2\text{I}_{7.6}$, $\text{Cu}_{0.7}\text{AgBi}_2\text{I}_{7.7}$, and $\text{CuAgBi}_2\text{I}_8$ films at the bottom and CuI upper layer in a sealed Teflon-lined stainless autoclave. This pure phase $\text{CuAgBi}_2\text{I}_8$ powder was prepared by spin coating and annealing of iodide solution. The obtained samples were characterized by XRD. Figure 1b shows the XRD patterns of $\text{Cu}_a\text{Ag}_{m1}\text{Bi}_{m2}\text{I}_n/\text{CuI}$ films, $\text{CuAgBi}_2\text{I}_8$ powder and the calculated structure by material studio (MS). These peaks at 22.8° , 25.2° , 29.7° , 41.5° should be assigned to the F-43 m cubic lattice of CuI (JCPDS No. 96–101-1240), indicating that a layer of CuI forms on the surface of $\text{CuAgBi}_2\text{I}_8$ film

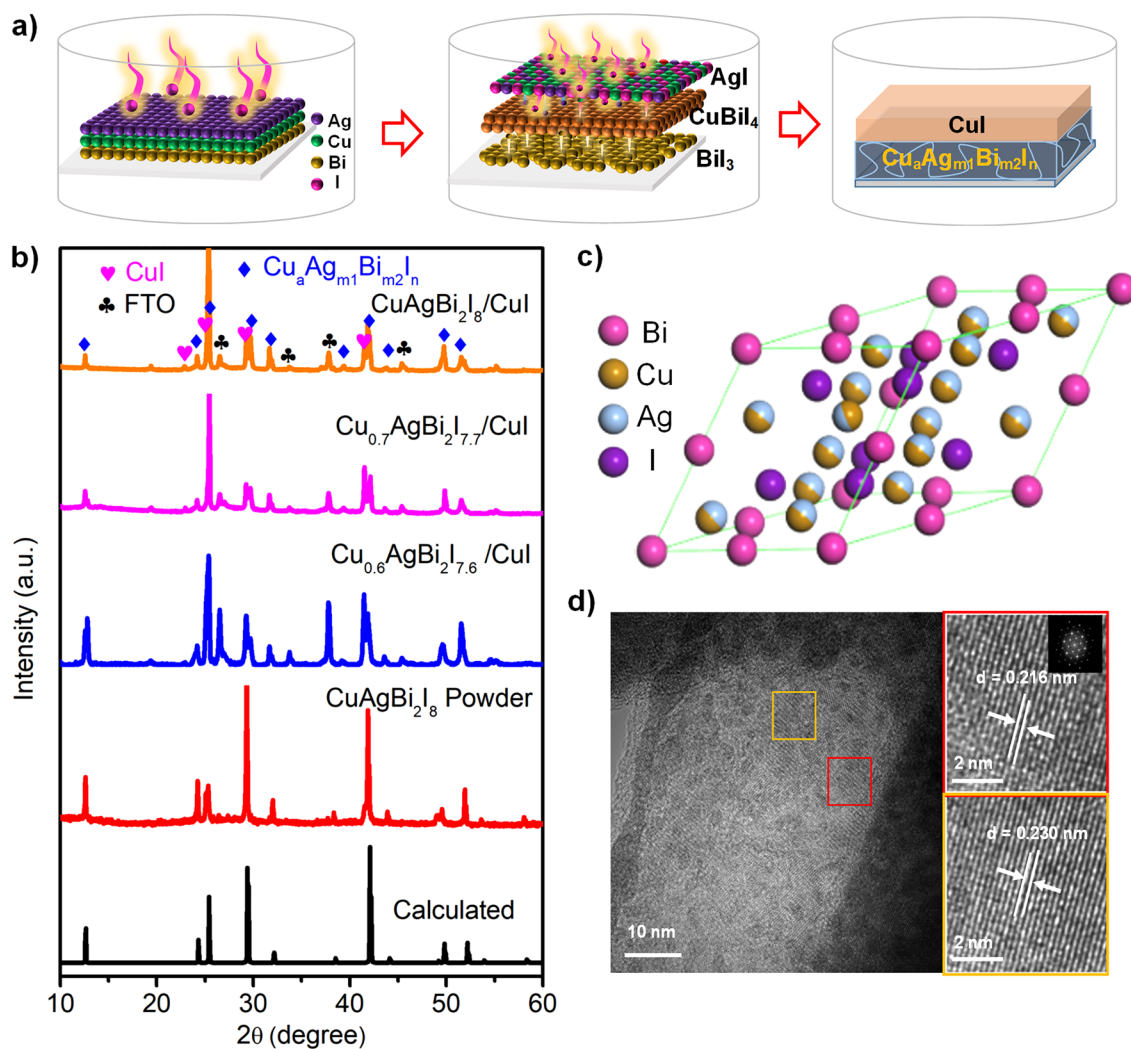


Fig. 1 **a** Schematic of $\text{Cu}_a\text{Ag}_{m1}\text{Bi}_{m2}\text{I}_n/\text{CuI}$ by the gas–solid-phase diffusion-induced direct metal surface elemental reaction (DMSER) of copper–silver–bismuth–iodine at a low temperature through tuning the Cu/Bi/Ag ratio. **b** XRD patterns spectra of $\text{Cu}_a\text{Ag}_{m1}\text{Bi}_{m2}\text{I}_n/\text{CuI}$, $\text{CuAgBi}_2\text{I}_8$ powder and calculated $\text{CuAgBi}_2\text{I}_8$ structure by MS software. **c** Crystal structure diagram of $\text{CuAgBi}_2\text{I}_8$ obtained by replacing Cu with Ag in the CuBi_4 structure. **d** HR-TEM image of $\text{CuAgBi}_2\text{I}_8$ and FFT pattern from red region and yellow region of $\text{CuAgBi}_2\text{I}_8$

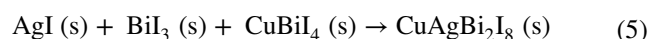
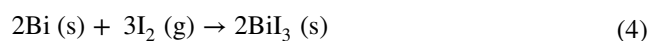
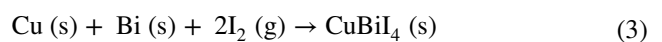
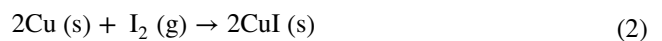
in the gas–solid-phase redox reaction, while the peaks at 12.6°, 24.1°, 25.5°, 29.1°, 38.6°, 42.8°, 49.7°, and 51.5° should be attributed to (111), (311), (222), (400), (333), (440), (622), and (444) planes of the relevant cubic ($Fd\bar{3}m$) phases of the $\text{CuAgBi}_2\text{I}_8$ quaternary compound. The structure of $\text{CuAgBi}_2\text{I}_8$ was obtained by replacing half of the Cu atoms with Ag atoms in CuBiI_4 structure (ICSD No. 71533) (Fig. 1c), which is distinct with the alternating layer structure of $\text{Cu}_2\text{AgBiI}_6$ with both octahedral and tetrahedral sites filled with Cu^+ , Ag^+ , Bi^{3+} , or I^- ions [20].

To clarify the structure difference between $\text{CuAgBi}_2\text{I}_8$ and $\text{Cu}_2\text{AgBiI}_6$, the upper CuI layer was etched by diluted HNO_3 firstly. As shown in cross-sectional SEM images (Figs. S4–S6), the $\text{Cu}_a\text{Ag}_{m1}\text{Bi}_{m2}\text{I}_n/\text{CuI}$ bilayer structure can transfer to single $\text{Cu}_a\text{Ag}_{m1}\text{Bi}_{m2}\text{I}_n$ layer after removing CuI by diluted HNO_3 etching. Compared with the reported $\text{Cu}_2\text{AgBiI}_6$ structure [18, 29, 30], the typical peaks of $\text{CuAgBi}_2\text{I}_8$ at $2\theta = 24.1^\circ$, 42.8° , and 51.5° shifted gradually to lower degrees (Fig. S7a), further confirming that the structure of $\text{CuAgBi}_2\text{I}_8$ is different from that of $\text{Cu}_2\text{AgBiI}_6$. The high-resolution transmission electron microscopy (HR-TEM) image of $\text{CuAgBi}_2\text{I}_8$ is shown in Fig. 1d. The clearly interplanar lattice spacings of 0.216 and 0.230 nm are indexed to crystal planes (440) and (333) of $\text{CuAgBi}_2\text{I}_8$, respectively. Therefore, the $\text{CuAgBi}_2\text{I}_8$ compound was successfully obtained. In the same preparation process, we regulate the ratio of Cu/Bi/Ag to prepared $\text{Cu}_{0.6}\text{AgBi}_2\text{I}_{7.6}$, $\text{Cu}_{0.7}\text{AgBi}_2\text{I}_{7.7}$ compound film. According to the XRD pattern of $\text{Cu}_a\text{Ag}_{m1}\text{Bi}_{m2}\text{I}_n$ films before and after etching (Fig. 1b and S7b), the peak positions of $\text{Cu}_{0.6}\text{AgBi}_2\text{I}_{7.6}$, $\text{Cu}_{0.7}\text{AgBi}_2\text{I}_{7.7}$, and $\text{CuAgBi}_2\text{I}_8$ have not changed except for the relative strength. Moreover, we further carried out a series of control experiments and compared the binary and ternary compounds with $\text{CuAgBi}_2\text{I}_8$ compound by XRD patterns (Fig. S8). The results show that there are no other phases in the absorption layer, and the absorption layer should be a single phase.

XPS was carried out to further investigate the composition of the $\text{Cu}_a\text{Ag}_{m1}\text{Bi}_{m2}\text{I}_n$ film after etching. The full XPS survey shows that all the expected elements Cu, Ag, Bi, and I were observed on the $\text{CuAgBi}_2\text{I}_8$ film after etching in Fig. S9. From the XPS spectra of Cu 2p of $\text{CuAgBi}_2\text{I}_8$ film and superficial CuI (Fig. S10), the two peaks with binding energies of 952.2 eV ($2p_{1/2}$) and 932.2 eV ($2p_{3/2}$) were observed obviously. The splitting of the spin orbit components is 20.1 eV, which is in accord with Cu^+ [31, 32]. Furthermore, the Cu 2p peak positions of $\text{CuAgBi}_2\text{I}_8$ film are consistent

with CuI, indicating that Cu^+ is present in both CuI layer and $\text{CuAgBi}_2\text{I}_8$ layer. The Bi $4f_{5/2}$ and Bi $4f_{7/2}$ peaks at binding energies of 159.0 and 164.3 eV (Fig. S11) are associated with the iodide-bound bismuth (III) [33]. The Ag 3d spin orbitals ($3d_{5/2}$ at 368.2 eV and $3d_{3/2}$ at 374.2 eV) with doublet separation of 6.0 eV can be assigned to Ag(I) (Fig. S12) [32]. Interestingly, the I core-level spectra show that the I $3d_{3/2}$ and $3d_{5/2}$ binding energies of $\text{CuAgBi}_2\text{I}_8$ shift 0.4 eV to the left in comparison to the CuI, revealing of the iodide-bound bismuth (Fig. S13). From the Raman spectra of $\text{Cu}_{0.6}\text{AgBi}_2\text{I}_{7.6}$, $\text{Cu}_{0.7}\text{AgBi}_2\text{I}_{7.7}$ and $\text{CuAgBi}_2\text{I}_8$ thin films (Fig. S14), the observed peak at 111.1 and 151.7 cm^{-1} should be assigned to $\text{Cu}_a\text{Ag}_{m1}\text{Bi}_{m2}\text{I}_n$ [20]. Interestingly, the peak position at 151.7 cm^{-1} never changes as the proportion of Cu/Ag/Bi elements, providing the further proof that the modified $\text{Cu}_a\text{Ag}_{m1}\text{Bi}_{m2}\text{I}_n$ quaternary compound should have the same crystal structure.

The evolution mechanism of $\text{CuAgBi}_2\text{I}_8/\text{CuI}$ bilayer structure was studied by a series of controlled experiments. From the XRD patterns of $\text{CuAgBi}_2\text{I}_8$ compounds at different reaction time (Fig. S15), the typical peaks of CuBiI_4 , CuI, BiI_3 , and AgI could be found after one hour of reaction. When the reaction time was extended to 6 h, these peaks of $\text{CuAgBi}_2\text{I}_8$, CuBiI_4 , CuI, BiI_3 , and AgI coexisted on the XRD pattern. After 24 h of reaction, the pure $\text{Cu}_a\text{Ag}_{m1}\text{Bi}_{m2}\text{I}_n/\text{CuI}$ bilayer structure was formed. The proposed reaction equation is as follows:



The standard electrode potentials of Cu, Ag, and Bi are given by: $E^\circ (\text{Ag}^+/\text{Ag}) = 0.80\text{V}$, $E^\circ (\text{Cu}^+/\text{Cu}) = 0.52\text{V}$ and $E^\circ (\text{Bi}^{3+}/\text{Bi}) = 0.31\text{V}$, respectively. Thus, the order of Bi, Ag, and Cu metal activation is $\text{Bi} > \text{Cu} > \text{Ag}$. Since Bi has the highest metal activation, we put it at the bottom to ensure that the reaction is complete. Due to the moderate activation of Cu, we tend to place the Cu under the Ag layer. As a result, a layer of CuI was formed on the $\text{CuAgBi}_2\text{I}_8$ indicating that there is a phenomenon of outward diffusion of Cu and inward diffusion of Ag driven by potential difference.

The outer layer of Ag and the middle layer of Cu can firstly react with I_2 gas to form AgI and CuI, respectively. Secondly, Bi and the extra Cu could further react with I_2 gas to afford $CuBiI_4$ during the atomic mutual diffusion. Thirdly, the BiI_3 was formed by the reaction of the residual Bi and I_2 . Finally, the generated BiI_3 , AgI, and $CuBiI_4$ were combined to form quaternary $CuAgBi_2I_8$ compound film at the bottom. Therefore, the $CuAgBi_2I_8/CuI$ bilayer structure was formed mainly by the atomic mutual diffusion of Cu, Bi and Ag during the redox reaction.

To determine the two-layered structure, scanning electron microscopy with energy-dispersive X-ray (SEM–EDX) was employed in characterization of morphology and composition analysis. As shown on the top-view SEM images (Fig. 2a, b, c), with the increase in the proportion of Cu in the compound, the upper grains gradually become larger and fuller, indicating the increase in Cu content can promote CuI growth. On the cross-sectional SEM images (Fig. 2d, e, f), the continuous and dense $Cu_aAg_{m1}Bi_{m2}I_n$ and CuI bilayer structure can be obviously observed. The thickness of the top and the bottom layers was measured, about 550 and 480 nm for $Cu_{0.6}AgBi_2I_{7.6}/CuI$, about 490 and 630 nm for $Cu_{0.7}AgBi_2I_{7.7}/CuI$, and about 690 and 800 nm

for $CuAgBi_2I_8/CuI$ film, respectively. Take $CuAgBi_2I_8$ as an example, each layer of metal is about 60–180 nm, and the total sputtering thickness of Cu, Ag, and Bi is over 300 nm. On the one hand, to react with these metals, at least 600 nm of stacked iodine atoms is required since iodine atoms are approximately twice the total amount of Cu–Ag–Bi metals in terms of the atomic ratio of $CuAgBi_2I_8$ chemical formula. Therefore, the total thickness of Cu–Ag–Bi–I compounds may reach about 900 nm. On the other hand, the density difference between the metal and the compound must be taken into the account. Metals usually are denser than compounds. For example, Cu and CuI densities are about 9.0 and 5.6 g cm⁻³, respectively. And Bi and BiI_3 densities are about 9.8 and 5.8 g cm⁻³, respectively. If the density of the metal is 1.6 times that of the compound, the total thicknesses of Cu–Ag–Bi–I compounds are roughly estimated to be 1440 nm, which is consistent with the observed thickness of $Cu_aAg_{m1}Bi_{m2}I_n/CuI$ films (1490 nm). Therefore, the thicknesses of Cu–Ag–Bi–I compounds and CuI are both over 400 nm.

The average composition of $Cu_{0.6}AgBi_2I_{7.6}$, $Cu_{0.7}AgBi_2I_{7.7}$, and $CuAgBi_2I_8$ was calculated statistically

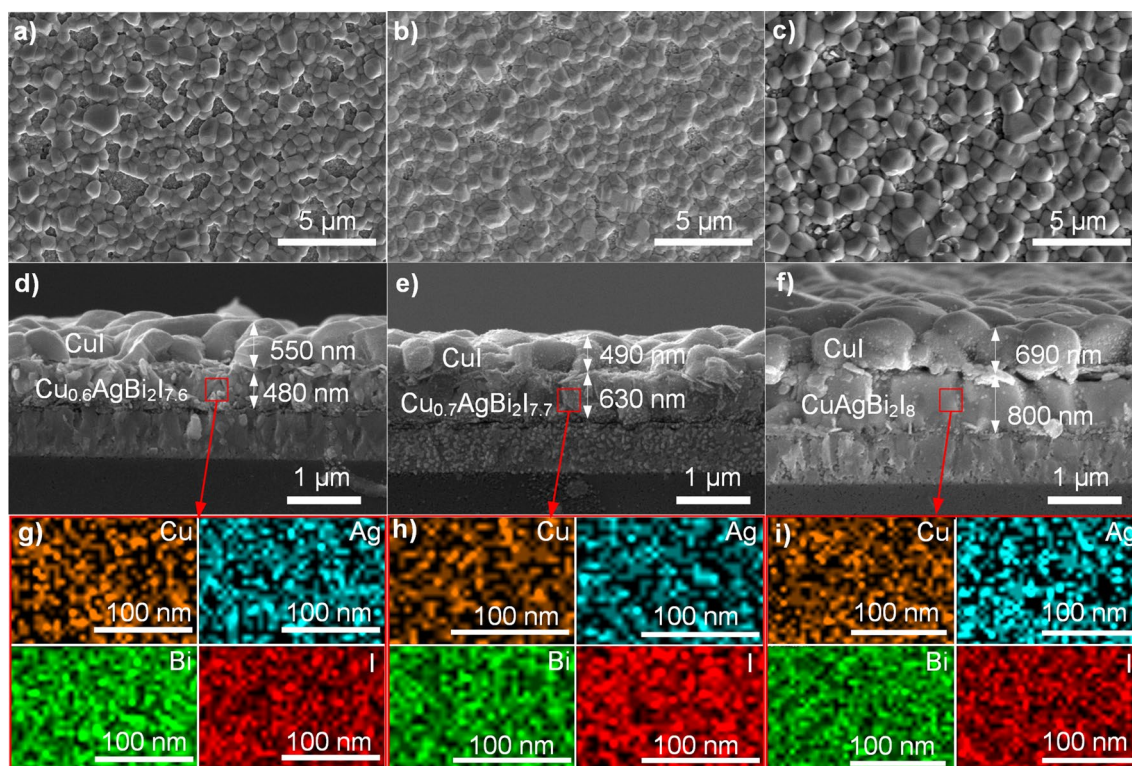


Fig. 2 Top-view and cross-sectional SEM images. **a, d** for $Cu_{0.6}AgBi_2I_{7.6}$, **b, e** for $Cu_{0.7}AgBi_2I_{7.7}$, **c, f** for $CuAgBi_2I_8$ thin films on FTO substrates, respectively. SEM mapping images of Cu, Ag, Bi, and I elements for **g** $Cu_{0.6}AgBi_2I_{7.6}$, **h** $Cu_{0.7}AgBi_2I_{7.7}$, and **i** $CuAgBi_2I_8$

by SEM–EDX for no less than three regions (Tables S1–S3). The Ag/Bi ratio in all $\text{Cu}_a\text{Ag}_{m1}\text{Bi}_{m2}\text{I}_n$ is closed to 1:2. The SEM–EDX mapping images show a uniform distribution of Cu, Ag, Bi, and I elements (Fig. 2g, h, i). A small amount of Ag^+ remained in the upper CuI layer. It is worth noting that the iodine content detected by EDX was lower than the expected value, which is attributed to the loss of iodine under the strong electron beam irradiation [23]. To further demonstrate the chemical composition, we scraped the powders of $\text{Cu}_a\text{Ag}_{m1}\text{Bi}_{m2}\text{I}_n$ (after etching) from FTO glass for inductively coupled plasma (ICP) and XPS tests. ICP results show that the atomic percentage of Cu, Ag, Bi, and I in $\text{CuAgBi}_2\text{I}_8$ is 9.70%, 8.41%, 17.4%, and 64.5% (Table S4), respectively. Thus, the composition of $\text{CuAgBi}_2\text{I}_8$ sample should be $\text{Cu}_{1.1}\text{Ag}_{1.0}\text{Bi}_{2.1}\text{I}_{7.7}$ by ICP measurement. At the same time, the compositions of $\text{Cu}_{0.7}\text{AgBi}_2\text{I}_{7.7}$ and $\text{Cu}_{0.6}\text{AgBi}_2\text{I}_{7.6}$ samples were measured to be $\text{Cu}_{0.69}\text{Ag}_{1.0}\text{Bi}_{1.8}\text{I}_{8.1}$ and $\text{Cu}_{0.58}\text{Ag}_{1.0}\text{Bi}_{2.0}\text{I}_{8.1}$, respectively, which are in line with the SEM–EDX results. The semi-quantitative analysis results of XPS also show that the atomic ratio of Ag to Bi is close to 1:2, which further proves the correctness of these compositions of

$\text{Cu}_a\text{Ag}_{m1}\text{Bi}_{m2}\text{I}_n$ (Table S5). Therefore, the $\text{Cu}_a\text{Ag}_{m1}\text{Bi}_{m2}\text{I}_n/\text{CuI}$ two-layered structure on the FTO was prepared successfully. The obtained CuI layer can be as a natural hole transport material of $\text{Cu}_a\text{Ag}_{m1}\text{Bi}_{m2}\text{I}_n$ absorption layer, which have excellent interfacial contact with the bottom layer [34].

3.2 Optical Properties of $\text{Cu}_a\text{Ag}_{m1}\text{Bi}_{m2}\text{I}_n$ Films

The optical properties of $\text{Cu}_a\text{Ag}_{m1}\text{Bi}_{m2}\text{I}_n$ films after etching were characterized by UV–vis absorption spectra, TRPL decay curves, and transient surface photovoltage (TSPV) curves. As shown in Fig. 3a, with the increase in Cu content, the absorption edge shows red shift. According to the Tauc plot (Fig. 3b), the lowest value of bandgap is about 1.78 eV, 0.28 eV lower than the reported 2.06 eV [20]. Herz et al. [21] once tried to adjust the ratio of Cu by controlling the ratio of Ag/Bi to 1:1 and found that the bandgap only shifts by 0.05 eV from 2.05 eV for $x=0$ (AgBi_4) down to 2.00 eV for $x=0.6$ ($\text{Cu}_6\text{AgBi}_{10}$). Thus, Cu content regulation cannot lead to such a large bandgap shift

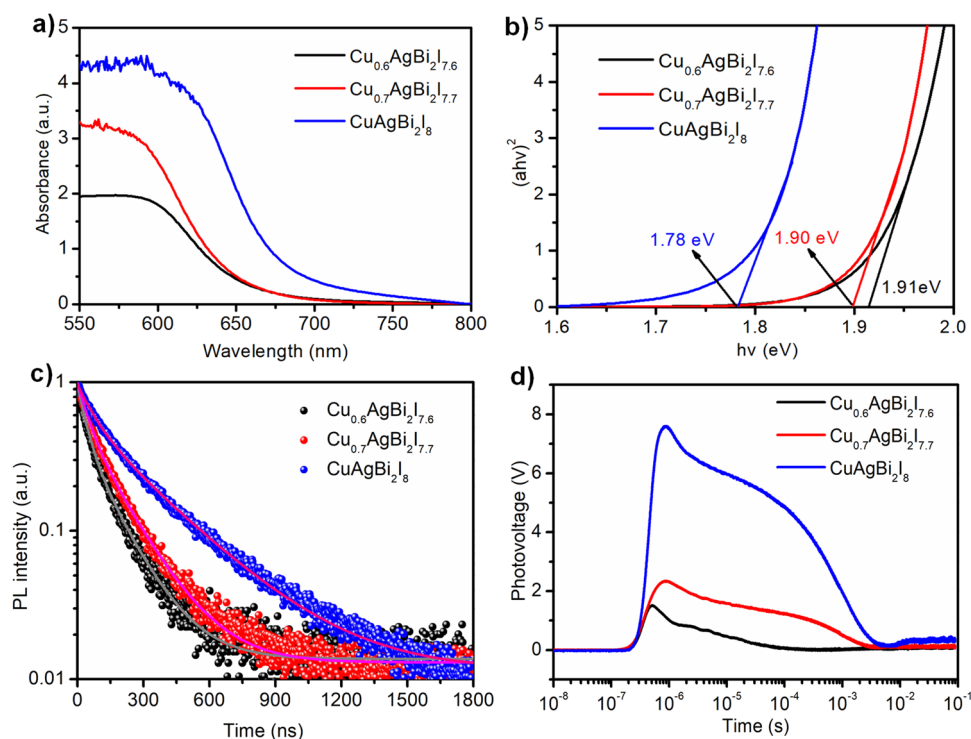


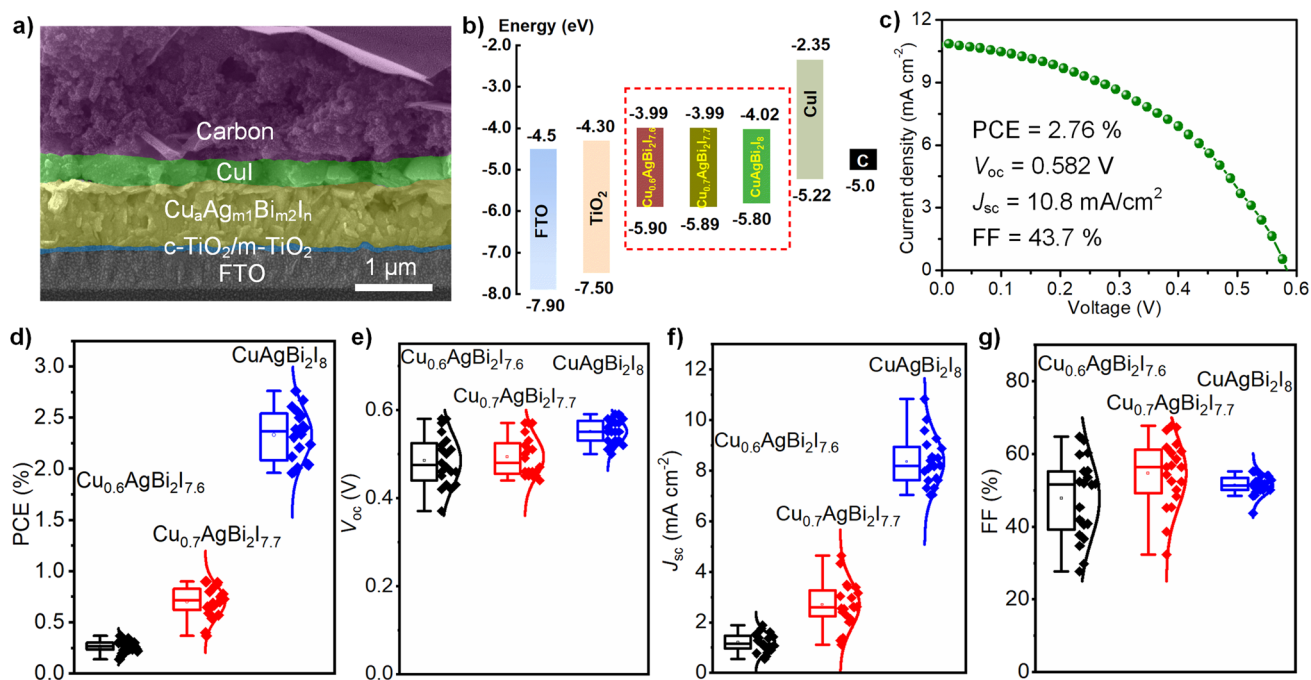
Fig. 3 **a** UV–vis absorption spectra of $\text{Cu}_a\text{Ag}_{m1}\text{Bi}_{m2}\text{I}_n$ films after etching. **b** Corresponding $(ahv)^2$ vs energy ($h\nu$) curves of $\text{Cu}_a\text{Ag}_{m1}\text{Bi}_{m2}\text{I}_n$ films after etching. **c** TRPL decay curves and **d** TSPV curves of $\text{Cu}_a\text{Ag}_{m1}\text{Bi}_{m2}\text{I}_n$ films after etching

(0.28 eV). The modification of the ratio of Ag to Bi (atomic ratio Ag/Bi = 1:2) should play a key role on the bandgap regulation strategy. TRPL decay measurements show that the average carrier lifetime (τ_{ave}) increased from 81.3 ns for $\text{Cu}_{0.6}\text{AgBi}_2\text{I}_{7.6}$ film to 201 ns for $\text{CuAgBi}_2\text{I}_8$ film (Fig. 3c, Table S6). The PL lifetime of $\text{CuAgBi}_2\text{I}_8$ film is about 6 times that of the reported $\text{Cu}_2\text{AgBiI}_6$ film, indicating that the $\text{CuAgBi}_2\text{I}_8$ film has more advantages in charge separation. TSPV measurements of $\text{Cu}_a\text{Ag}_{m1}\text{Bi}_{m2}\text{I}_n$ films were carried out by using a 355-nm pulsed laser with a pulse width of 4 ns in according to the reported method [35]. A positive signal means that these $\text{Cu}_a\text{Ag}_{m1}\text{Bi}_{m2}\text{I}_n$ films have n-type semiconductor properties due to the accumulation of photoinduced electrons at the surface (Fig. 3d) [17, 35]. The photoinduced electron recombination time of $\text{CuAgBi}_2\text{I}_8$ film is about 5.48×10^{-3} s at the highest decay slope, which is higher than those of $\text{Cu}_{0.6}\text{AgBi}_2\text{I}_{7.6}$ film (2.91×10^{-3} s) and $\text{Cu}_{0.7}\text{AgBi}_2\text{I}_{7.7}$ (3.16×10^{-4} s). The photovoltage of $\text{CuAgBi}_2\text{I}_8$ film is the biggest among the $\text{Cu}_a\text{Ag}_{m1}\text{Bi}_{m2}\text{I}_n$ films, indicating of the highest photoinduced charge carrier concentration (Table S7). Charge carrier mobilities play a significant role in the performance of photovoltaic

devices. We determined effective charge-carrier mobilities of $\text{CuAgBi}_2\text{I}_8$ by using Hall effect measurement. The value for the electron-hole total mobility is $2.80 \text{ cm}^2\text{V}^{-1} \text{ s}^{-1}$ (Table S8), which is higher than that of double perovskite $\text{Cs}_2\text{AgBiBr}_6$ ($0.8 \text{ cm}^2\text{V}^{-1} \text{ s}^{-1}$) [36] and $\text{Cu}_2\text{AgBiI}_6$ ($1.7 \text{ cm}^2\text{V}^{-1} \text{ s}^{-1}$) [20, 25]. Charge carrier diffusion length is calculated by equation of $L_D = \sqrt{\tau\mu_e kT/q}$, and the estimated value is 3.8 μm , indicating a preferable charge carrier diffusion length. Therefore, the $\text{CuAgBi}_2\text{I}_8$ film with a two-layered structure has the best dynamical behavior of photogenerated carriers, suggesting that it has a great application potential as an absorption layer in solar cell devices.

3.3 Performance of $\text{Cu}_a\text{Ag}_{m1}\text{Bi}_{m2}\text{I}_n$ Solar Cells

We assembled the $\text{CuAgBi}_2\text{I}_8$ film as an absorption layer into a planar heterojunction photovoltaic cell. Figure 4a shows the schematic cross-sectional view of the $\text{Cu}_a\text{Ag}_{m1}\text{Bi}_{m2}\text{I}_n$ solar cells. The n-i-p type cell has a structure of FTO/c-TiO₂/m-TiO₂/ $\text{Cu}_a\text{Ag}_{m1}\text{Bi}_{m2}\text{I}_n$ /CuI/carbon. A layer of activated carbon is deposited on $\text{Cu}_a\text{Ag}_{m1}\text{Bi}_{m2}\text{I}_n$ as



a bifunctional film with a work function (-5.0 eV) close to gold (-5.1 eV), which can be effectively used for hole extraction and collection [37, 38]. In addition, carbon electrodes are very stable, processable, and inexpensive. The band structure of $\text{Cu}_a\text{Ag}_{m_1}\text{Bi}_{m_2}\text{I}_n$ was calculated through their UPS spectra (Figs. S16–S18) and UV–vis absorption spectra (Fig. 3a). As shown in Fig. 4b, band energy levels of the FTO, TiO_2 , $\text{Cu}_a\text{Ag}_{m_1}\text{Bi}_{m_2}\text{I}_n$, and carbon layers represent the smooth electron transport from the $\text{Cu}_a\text{Ag}_{m_1}\text{Bi}_{m_2}\text{I}_n$ to the TiO_2 in the conduction band and hole extraction from the $\text{Cu}_a\text{Ag}_{m_1}\text{Bi}_{m_2}\text{I}_n$ to the CuI and carbon electrode in the valence band. Figure 4c shows the J–V curve of $\text{CuAgBi}_2\text{I}_8/\text{CuI}$ based solar cell device. All the $\text{Cu}_a\text{Ag}_{m_1}\text{Bi}_{m_2}\text{I}_n$ solar cells with different ratio of Cu/Ag/Bi were also fabricated, as shown in Fig. S19. The corresponding photovoltaic parameters of the $\text{Cu}_a\text{Ag}_{m_1}\text{Bi}_{m_2}\text{I}_n$ solar cell devices with an active area of 0.04 cm^2 , including the short-circuit density (J_{sc}), open-circuit voltage (V_{oc}), fill factor (FF), and PCE, are presented in Fig. 4c and Table S9.

The PCE of $\text{CuAgBi}_2\text{I}_8$ solar cell is as high as 2.76%, which is highest value reported for this class of materials [20, 22, 24]. In detail, the $\text{CuAgBi}_2\text{I}_8$ solar cell has higher V_{oc} (0.582 V) and J_{sc} (up to 10.8 mA cm^{-2}) than the reported $\text{Cu}_2\text{AgBiI}_6$ devices (Table S9). The J_{sc} data were almost twice as high as the reported (5.3 mA cm^{-2}) [24]. All these are closely related to the bandgap regulation engineering, which enhances the harvest of light owing to the reduction in the bandgap. On the other hand, the CuI layer as a natural hole transport layer is beneficial to enhancing the hole extraction. As shown in Fig. S20, our $\text{CuAgBi}_2\text{I}_8$ devices show slight J–V hysteresis, which may be due to the imbalanced charge transportation at interfaces and non-radiative recombination [39]. To demonstrate the reproducibility and statistic properties, about 20 devices were fabricated and characterized as shown in Fig. 4d, e, f, g. The PCE statistics are distributed over a small range with an average value of 2.32%. This high photovoltaic performance of $\text{CuAgBi}_2\text{I}_8$ should be due to the growing of current density (J_{sc}) caused by the regulation of Cu/Ag/Bi metal proportion (Fig. 4f). From the IPCE spectrum in Fig. S21, $\text{CuAgBi}_2\text{I}_8$ device has a wide spectral response in the wavelength range of 300–700 nm. An integrated current of $\text{CuAgBi}_2\text{I}_8$ is obtained from the IPCE spectra of the best cell. To furtherly evaluate the stability of $\text{Cu}_a\text{Ag}_{m_1}\text{Bi}_{m_2}\text{I}_n$ solar cell, the J–V curves of $\text{CuAgBi}_2\text{I}_8$ devices were recorded after 100 days in air (Fig.

S22a). The unencapsulated $\text{Cu}_a\text{Ag}_{m_1}\text{Bi}_{m_2}\text{I}_n$ solar cell retains nearly 63% of its initial PCE after 100 days in air. The crystal structure of $\text{CuAgBi}_2\text{I}_8$ had not changed after 100 days in air by the determination of the XRD pattern (Fig. S22b).

4 Conclusions

In summary, we fabricated a series of $\text{Cu}_a\text{Ag}_{m_1}\text{Bi}_{m_2}\text{I}_n$ films with self-generated CuI hole transport layer via the gas–solid-phase reaction of copper–silver–bismuth–iodine elements at low temperature. By tuning the sputtered Cu/Ag/Bi metal film thickness, the bandgap of the corresponding quaternary compounds could be reduced from 2.06 to 1.78 eV. Interestingly, both a continuous and dense $\text{Cu}_a\text{Ag}_{m_1}\text{Bi}_{m_2}\text{I}_n$ light absorption layer and a CuI hole transport layer could form simultaneously due to the strong atomic diffusion effect of Bi, Cu, and Ag during the redox reaction process. The $\text{CuAgBi}_2\text{I}_8$ solar cell with an FTO/ $\text{TiO}_2/\text{Cu}_a\text{Ag}_{m_1}\text{Bi}_{m_2}\text{I}_n/\text{CuI}/\text{carbon}$ structure delivers an optimum PCE of 2.76% with an improved J_{sc} of 10.8 mA cm^{-2} , which is the highest reported so far. This work will pave the way on the development of fabricating a new type environmentally friendly $\text{Cu}_a\text{Ag}_{m_1}\text{Bi}_{m_2}\text{I}_n$ inorganic photovoltaic materials. However, we have to admit that the current PCE is still too low in comparison to lead-based devices. At the present stage, we are not skilled in the dynamic control of this gas–solid reaction, with poor crystallinity, small grains, and many defects, leading to serious charge recombination. On the other hand, the device structure is only preliminary exploration, resulting that the interface charge transfer is not optimal. In addition, the bandgap has not reduced to an ideal range (1.4–1.6 eV). In the future, the photovoltaic properties of $\text{Cu}_a\text{Ag}_{m_1}\text{Bi}_{m_2}\text{I}_n$ thin film materials will be improved by introducing the coordination system and adjusting reaction activation energy to promote the generation of large crystal grains with little defects. By further adjusting the ratio of Cu, Ag, Bi, and I to tune the ratio of tetrahedral/octahedral lattice structure, the bandgap of $\text{Cu}_a\text{Ag}_{m_1}\text{Bi}_{m_2}\text{I}_n$ will be further adjusted to the ideal range.

Acknowledgements This work was financially supported by National Natural Science Foundation of China (Grant No. 52072327, 62074052, 61874159); Zhongyuan Thousand Talents (Zhongyuan Scholars) Program of Henan Province (202101510004); Higher Education and Teaching Reformation

Project (2014SJGLX064); Academic Degrees & Graduate Education Reform Project of Henan Province (2021SJGLX060Y); Key research and development projects of Universities in Henan Province (20A140026); the Scientific Research Innovation Team of Xuchang University (2022CXTD008); Science and Technology Project of Henan Province (222102230009). L. Ding thanks the National Key Research and Development Program of China (2022YFB3803300), the open research fund of Songshan Lake Materials Laboratory (2021SLABFK02), and the National Natural Science Foundation of China (21961160720).

Funding Open access funding provided by Shanghai Jiao Tong University.

Open Access This article is licensed under a Creative Commons Attribution 4.0 International License, which permits use, sharing, adaptation, distribution and reproduction in any medium or format, as long as you give appropriate credit to the original author(s) and the source, provide a link to the Creative Commons licence, and indicate if changes were made. The images or other third party material in this article are included in the article's Creative Commons licence, unless indicated otherwise in a credit line to the material. If material is not included in the article's Creative Commons licence and your intended use is not permitted by statutory regulation or exceeds the permitted use, you will need to obtain permission directly from the copyright holder. To view a copy of this licence, visit <http://creativecommons.org/licenses/by/4.0/>.

Supplementary Information The online version contains supplementary material available at <https://doi.org/10.1007/s40820-023-01033-5>.

References

1. W. Xiang, W. Tress, Review on recent progress of all-inorganic metal halide perovskites and solar cells. *Adv. Mater.* **31**, e1902851 (2019). <https://doi.org/10.1002/adma.201902851>
2. H. Li, W. Zhang, Perovskite tandem solar cells: from fundamentals to commercial deployment. *Chem. Rev.* **120**, 9835–9950 (2020). <https://doi.org/10.1021/acs.chemrev.9b00780>
3. S. Bellani, A. Bartolotta, A. Agresti, G. Calogero, G. Grancini et al., Solution-processed two-dimensional materials for next-generation photovoltaics. *Chem. Soc. Rev.* **50**, 11870–11965 (2021). <https://doi.org/10.1039/d1cs00106j>
4. X. Li, W. Zhang, X. Guo, C. Lu, J. Wei et al., Constructing heterojunctions by surface sulfidation for efficient inverted perovskite solar cells. *Science* **375**, 434–437 (2022). <https://doi.org/10.1126/science.abi5676>
5. N. Li, X. Niu, L. Li, H. Wang, Z. Huang et al., Liquid medium annealing for fabricating durable perovskite solar cells with improved reproducibility. *Science* **373**, 561–567 (2021). <https://doi.org/10.1126/science.abh3884>
6. W. Hui, L. Chao, H. Lu, F. Xia, Q. Wei et al., Stabilizing black-phase formamidinium perovskite formation at room temperature and high humidity. *Science* **371**, 1359–1364 (2021). <https://doi.org/10.1126/science.abf7652>
7. S. Chen, X. Dai, S. Xu, H. Jiao, L. Zhao et al., Stabilizing perovskite-substrate interfaces for high-performance perovskite modules. *Science* **373**, 902–907 (2021). <https://doi.org/10.1126/science.abi6323>
8. N. Li, X. Niu, Q. Chen, H. Zhou, Towards commercialization: the operational stability of perovskite solar cells. *Chem. Soc. Rev.* **49**, 8235–8286 (2020). <https://doi.org/10.1039/d0cs00573h>
9. Z. Xiao, K.Z. Du, W. Meng, D.B. Mitzi, Y. Yan, Chemical origin of the stability difference between copper(I)- and silver(I)-based halide double perovskites. *Angew. Chem. Int. Ed.* **56**, 12107–12111 (2017). <https://doi.org/10.1002/anie.201705113>
10. X. Yang, Y. Chen, P. Liu, H. Xiang, W. Wang et al., Simultaneous power conversion efficiency and stability enhancement of Cs₂AgBiBr₆ lead-free inorganic perovskite solar cell through adopting a multifunctional dye interlayer. *Adv. Funct. Mater.* **30**, 2001557 (2020). <https://doi.org/10.1002/adfm.202001557>
11. T. Cai, W. Shi, S. Hwang, K. Kobbekaduwa, Y. Nagaoka et al., Lead-free Cs₄CuSb₂Cl₁₂ layered double perovskite nanocrystals. *J. Am. Chem. Soc.* **142**, 11927–11936 (2020). <https://doi.org/10.1021/jacs.0c04919>
12. A.H. Slavney, L. Leppert, D. Bartesaghi, A. Gold-Parker, M.F. Toney et al., Defect-induced band-edge reconstruction of a bismuth-halide double perovskite for visible-light absorption. *J. Am. Chem. Soc.* **139**, 5015–5018 (2017). <https://doi.org/10.1021/jacs.7b01629>
13. M. Chen, M.-G. Ju, A.D. Carl, Y. Zong, R.L. Grimm et al., Cesium titanium (IV) bromide thin films based stable lead-free perovskite solar cells. *Joule* **2**, 558–570 (2018). <https://doi.org/10.1016/j.joule.2018.01.009>
14. X.G. Zhao, D. Yang, Y. Sun, T. Li, L. Zhang et al., Cu-In halide perovskite solar absorbers. *J. Am. Chem. Soc.* **139**, 6718–6725 (2017). <https://doi.org/10.1021/jacs.7b02120>
15. Z. Zhang, Q. Sun, Y. Lu, F. Lu, X. Mu et al., Hydrogenated Cs₂AgBiBr₆ for significantly improved efficiency of lead-free inorganic double perovskite solar cell. *Nat. Commun.* **13**, 3397 (2022). <https://doi.org/10.1038/s41467-022-31016-w>
16. X.G. Zhao, J.H. Yang, Y. Fu, D. Yang, Q. Xu et al., Design of lead-free inorganic halide perovskites for solar cells via cation-transmutation. *J. Am. Chem. Soc.* **139**, 2630–2638 (2017). <https://doi.org/10.1021/jacs.6b09645>
17. B. Zhang, Y. Lei, R. Qi, H. Yu, X. Yang et al., An in-situ room temperature route to CuBiI₄ based bulk-heterojunction perovskite-like solar cells. *Sci. China Mater.* **62**, 519–526 (2018). <https://doi.org/10.1007/s40843-018-9355-0>
18. F. Yu, L. Wang, K. Ren, S. Yang, Z. Xu et al., Cs-incorporated AgBiI₄ ruddorffite for efficient and stable solar cells. *ACS Sustain. Chem. Eng.* **8**, 9980–9987 (2020). <https://doi.org/10.1021/acssuschemeng.0c00496>
19. H.C. Sansom, G.F.S. Whitehead, M.S. Dyer, M. Zanella, T.D. Manning et al., AgBiI₄ as a lead-free solar absorber with potential application in photovoltaics. *Chem. Mater.* **29**,

- 1538–1549 (2017). <https://doi.org/10.1021/acs.chemmater.6b04135>
20. H.C. Sansom, G. Longo, A.D. Wright, L.R.V. Buizza, S. Mahesh et al., Highly absorbing lead-free semiconductor $\text{Cu}_2\text{AgBiI}_6$ for photovoltaic applications from the quaternary CuI-AgI-BiI_3 phase space. *J. Am. Chem. Soc.* **143**, 3983–3992 (2021). <https://doi.org/10.1021/jacs.1c00495>
21. L.R.V. Buizza, H.C. Sansom, A.D. Wright, A.M. Ulatowski, M.B. Johnston et al., Interplay of structure, charge-carrier localization and dynamics in copper-silver-bismuth-halide semiconductors. *Adv. Funct. Mater.* **32**, 2108392 (2021). <https://doi.org/10.1002/adfm.202108392>
22. F. Zhang, Z. Hu, B. Zhang, Z. Lin, J. Zhang et al., Low-temperature solution-processed $\text{Cu}_2\text{AgBiI}_6$ films for high performance photovoltaics and photodetectors. *ACS Appl. Mater. Interfaces* **14**, 18498–18505 (2022). <https://doi.org/10.1021/acscami.2c01481>
23. G.K. Grandhi, B. Al-Anesi, H. Pasanen, H. Ali-Loytty, K. Lahtonen et al., Enhancing the microstructure of perovskite-inspired Cu-Ag-Bi-I absorber for efficient indoor photovoltaics. *Small* **18**, e2203768 (2022). <https://doi.org/10.1002/sml.202203768>
24. N. Pai, M. Chatti, S.O. Furer, A.D. Scully, S.R. Raga et al., Solution processable direct bandgap copper-silver-bismuth iodide photovoltaics: Compositional control of dimensionality and optoelectronic properties. *Adv. Energy Mater.* **12**, 2201482 (2022). <https://doi.org/10.1002/aenm.202201482>
25. L.R.V. Buizza, A.D. Wright, G. Longo, H.C. Sansom, C.Q. Xia et al., Charge-carrier mobility and localization in semiconducting $\text{Cu}_2\text{AgBiI}_6$ for photovoltaic applications. *ACS Energy Lett.* **6**, 1729–1739 (2021). <https://doi.org/10.1021/acscenergyl.1c00458>
26. H. Yu, B. Zhang, R. Qi, N. Qu, C. Zhao et al., Gradient formation and charge carrier dynamics of CuBiI_4 based perovskite-like solar cells. *Sustain. Energy Fuels* **4**, 2800–2807 (2020). <https://doi.org/10.1039/c9se01288e>
27. Y. Lei, R. Qi, M. Chen, H. Chen, C. Xing et al., Microstructurally tailored thin $\beta\text{-Ag}_2\text{Se}$ films toward commercial flexible thermoelectrics. *Adv. Mater.* **34**, e2104786 (2022). <https://doi.org/10.1002/adma.202104786>
28. P. Dong, C. Zhao, Y. Lei, H. Song, S. Wu et al., Significant enhancement in optoelectronic properties of $\gamma\text{-Cu}_x\text{Ag}_{1-x}\text{I}$ films induced by highly (111)-preferred orientation and Cu content at room temperature. *Cryst. Growth Des.* **21**, 4038–4045 (2021). <https://doi.org/10.1021/acs.cgd.1c00334>
29. M. Keshavarz, E. Debroye, M. Ottesen, C. Martin, H. Zhang et al., Tuning the structural and optoelectronic properties of $\text{Cs}_2\text{AgBiBr}_6$ double-perovskite single crystals through alkali-metal substitution. *Adv. Mater.* **32**, e2001878 (2020). <https://doi.org/10.1002/adma.202001878>
30. Z. Li, S.R. Kavanagh, M. Napari, R.G. Palgrave, M. Abdi-Jalebi et al., Bandgap lowering in mixed alloys of $\text{Cs}_2\text{Ag}(\text{Sb}_x\text{Bi}_{1-x})\text{Br}_6$ double perovskite thin films. *J. Mater. Chem. A* **8**, 21780–21788 (2020). <https://doi.org/10.1039/d0ta07145e>
31. Y. Cui, M. Wang, P. Dong, S. Zhang, J. Fu et al., DMF-based large-grain spanning $\text{Cu}_2\text{ZnSn}(\text{S}_x\text{Se}_{1-x})_4$ device with a PCE of 11.76%. *Adv. Sci.* **9**, e2201241 (2022). <https://doi.org/10.1002/advs.202201241>
32. Y. Sun, P. Qiu, W. Yu, J. Li, H. Guo et al., N-Type surface design for p-type CZTSSe thin film to attain high efficiency. *Adv. Mater.* **33**, e2104330 (2021). <https://doi.org/10.1002/adma.202104330>
33. N. Pai, J. Lu, T.R. Gengenbach, A. Seeber, A.S.R. Chesman et al., Silver bismuth sulfioiodide solar cells: tuning optoelectronic properties by sulfide modification for enhanced photovoltaic performance. *Adv. Energy Mater.* **9**, 1803396 (2018). <https://doi.org/10.1002/aenm.201803396>
34. J.A. Christians, R.C. Fung, P.V. Kamat, An inorganic hole conductor for organo-lead halide perovskite solar cells. Improved hole conductivity with copper iodide. *J. Am. Chem. Soc.* **136**, 758–764 (2014). <https://doi.org/10.1021/ja411014k>
35. Y. Lei, L. Gu, W. He, Z. Jia, X. Yang et al., Intrinsic charge carrier dynamics and device stability of perovskite/ZnO mesostructured solar cells in moisture. *J. Mater. Chem. A* **4**, 5474–5481 (2016). <https://doi.org/10.1039/c6ta00614k>
36. E.M. Hutter, M.C. Gelvez-Rueda, D. Bartesaghi, F.C. Grozema, T.J. Savenije, Band-like charge transport in $\text{Cs}_2\text{AgBi}_{1-x}\text{Sb}_x\text{Br}_6$ and mixed antimony bismuth $\text{Cs}_2\text{AgBi}_{1-x}\text{Sb}_x\text{Br}_6$ halide double perovskites. *ACS Omega* **3**, 11655–11662 (2018). <https://doi.org/10.1021/acsomega.8b01705>
37. J. Liang, C. Wang, Y. Wang, Z. Xu, Z. Lu et al., All-inorganic perovskite solar cells. *J. Am. Chem. Soc.* **138**, 15829–15832 (2016). <https://doi.org/10.1021/jacs.6b10227>
38. A. Mei, X. Li, L. Liu, Z. Ku, T. Liu et al., A hole-conductor-free, fully printable mesoscopic perovskite solar cell with high stability. *Science* **345**, 295–298 (2014). <https://doi.org/10.1126/science.1254763>
39. D.H. Kang, N.G. Park, On the current-voltage hysteresis in perovskite solar cells: dependence on perovskite composition and methods to remove hysteresis. *Adv. Mater.* **31**, e1805214 (2019). <https://doi.org/10.1002/adma.201805214>

